Minimizing Roughness Induced Optical Losses for a Four-Terminal CdTe/Si Tandem Solar Cell

John Keil,[1] Bryan M. Cote,[1] Vinodh Chandrasekaran,[2] Andrei Los,[2] and Vivian E. Ferry[1,*]

[1] *Department of Chemical Engineering and Materials Science, University of Minnesota, Minneapolis, Minnesota 55455, USA*

[2] *First Solar Inc., 28101 Cedar Park Blvd., Perrysburg, Ohio 43551, USA*

(Received 15 December 2022; revised 8 March 2023; accepted 7 April 2023; published 4 May 2023)

With high photovoltaic efficiencies, low production costs, and long-term stability of single junction cells, CdTe/Si four-terminal tandem solar cells are promising devices for surpassing single junction Si solar cell efficiency limits. High sub-band-gap transmission in the top junction is crucial to reach high efficiencies. Here, we study the impact of surface roughness on transmission using experiments and simulations, showing that the as-deposited texture both increases backscattering and parasitic absorption compared to flat surfaces due to electric field concentration in mesoscale surface features. Adding the ethylene vinyl acetate interlayer increases transmittance by reducing the index contrast at the back transparent conductive oxide. We show that these roughness-induced losses can be overcome by including high index optical coatings as additional interlayers, resulting in increased transmission through the CdTe cell and Si bottom cell efficiency that is comparable to a flat reference device.

DOI: 10.1103/PRXEnergy.2.023004

I. INTRODUCTION

As single junction Si cells approach their performance limits, tandem architectures are becoming increasingly important in the drive for higher efficiencies [1–3]. Si is an advantageous choice for the bottom cell, given the technoeconomic benefits of the established Si photovoltaic industry [1,4,5]. Cadmium telluride (CdTe) is a promising candidate for the top subcell, as it is a proven material with high efficiency and long-term stability and can be mass produced for a low cost [6]. The band gaps of CdTe and Si are 1.5 and 1.12 eV, respectively, which allows near-infrared (NIR) light to transmit through the CdTe subcell and reach the Si subcell. To improve cell performance, CdTe is often alloyed with Se, which additionally makes the absorber band gap adjustable between approximately 1.38 eV (at approximately 40% Se) and 1.7 eV (pure CdSe). The combined benefits give CdTe/Si tandem cells advantages over other tandem systems like III-V/Si, which have high production costs [4], and perovskite/Si, which require improved stability and scalability [7]. For successful implementation, the tandem architecture must exceed the performance of the single junction device. Thus-far, CdTe solar cells epitaxially grown on Si cells have only yielded relatively low efficiencies of 17% [8]. On the other hand, high temperatures and aggressive chemistries involved in thin film CdTe device processing make direct deposition of these materials onto Si cells impractical [9–14].

Tamboli *et al*. predicted efficiencies in the range of 25%–30% if CdTe and silicon cells were electrically separated in the four-terminal mechanically stacked configuration schematically depicted in Fig. 1(a) [6]. This configuration removes complexity from the tandem cell electrical design, as the direct series electrical connection of the cells, which is usually achieved through a tunneling junction, is not required. Electrically separating the subcells makes perfect current matching unnecessary, which is a major design constraint for the two-terminal monolithically integrated devices [15,16]. In particular, Isah *et al*. [15] concluded that the maximum monolithic CdTe/Si tandem efficiency was obtained with a CdTe layer thinned down to 0.2 μm. Such thin absorbers tend to suffer from pinholes and shunting, more so when deposited on standard textured Si cells, making practical implementation of the design challenging [17]. Another disadvantage of the monolithic two-terminal tandem that is eliminated by the four-terminal mechanically stacked design is a strong sensitivity of the current generated by the bottom subcell to the incident solar spectrum. As a result, top and bottom subcell currents can be matched well for some climates and

*veferry@umn.edu

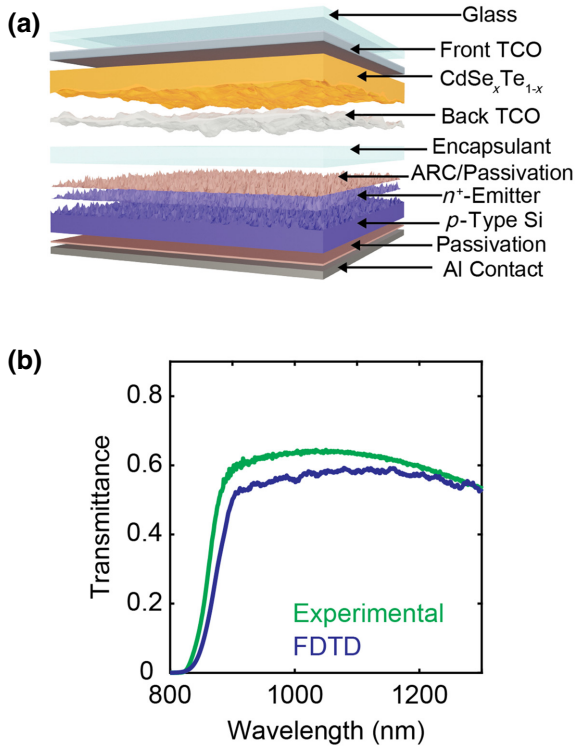

FIG. 1. (a) Illustration of a CdTe/Si four-terminal tandem solar cell (ARC is anti-reflection coating). (b) CdTe solar cell experimental and simulated transmittance.

seasons, while the matching becomes suboptimal for other climates and seasons, resulting in energy yield losses [18].

The optical challenges introduced with four-terminal tandem devices, however, require strategic optical design and photon management to achieve high efficiencies. Photon management is essential in tandem devices to best utilize both semiconductor absorbers and achieve high efficiencies and is especially important in four-terminal tandem configurations. The strategic selection of conductive layer materials, surface texture for improved light coupling, and thickness optimization to control absorption and reflection become especially important with tandem devices to minimize reflection and parasitic absorption losses [15,19,20]. In the CdTe/Si four-terminal configuration, sub-band-gap light not absorbed by the CdTe cell must be transmitted through the transparent front and back contacts of the CdTe layer, the encapsulant, and the top of the Si cell before it can be converted into electricity by the Si cell.

Achieving high transmission values therefore requires the use of both transparent back electrodes and understanding of the impact of surface roughness on light transmission. Previous studies on CdTe devices with transparent back contacts were successful at improving the NIR transmittance to about 70% [12,21,22], using relatively flat CdTe topography. The CdTe film preparation technique impacts on the surface topography and microstructure. Common CdTe film deposition techniques for photovoltaics include vapor transport deposition (VTD), thermal evaporation, close-space sublimation (CSS), and magnetron sputtering [9–12,22–29]. Among the techniques most suitable for industrial applications, VTD and CSS, VTD has key advantages, including high rates, low cost, smaller source areas, and decoupled substrate and source environments [9,11,23,25,28]. VTD produces high-quality polycrystalline CdTe films, and the grain size can be controlled by tuning the substrate temperature [28]. The impact of treatments such as $CdCl_2$ and heat on the electrical properties of CdTe cells is also well studied; these treatments lead to morphological changes, such as increased grain size and surface roughness, that affect NIR transparency [13,14,29–33].

However, the importance of surface roughness in the four-terminal device configuration, and the interaction between the surface texture and transparent electrodes, is not well characterized or understood. Here, we use a combination of simulations and experiments to understand and reduce roughness induced transparency losses in a CdTe/Si four-terminal device, with special attention paid to surface texture induced absorption enhancement in the transparent back contact. We also offer strategies to mitigate these losses through high index optical coatings and planarization.

II. RESULTS AND DISCUSSION

Figure 1(a) shows our assumed device configuration. The CdTe cell is assumed to have a planar front transparent conductive oxide (TCO); the absorber layer is comprised of VTD deposited $CdSe_xTe_{1-x}$, with surface roughness on the back interface; and a conformally grown back metal oxide based TCO is included as a rear conductive layer. In the full tandem configuration, this is followed by an encapsulant layer (ethylene vinyl acetate, or EVA) and a typical Si cell underneath. The refractive index of each layer is shown in Fig. S1 within the Supplemental Material [34].

$CdSe_xTe_{1-x}$ solar cell samples are received from First Solar Inc. without EVA encapsulation. The total sub-band-gap transmittance is measured by UV-vis spectrophotometry and plotted in Fig. 1(b). Finite-difference time-domain (FDTD) simulations are used to analyze the sub-band-gap transmittance of the $CdSe_xTe_{1-x}$ top cell in the proposed $CdSe_xTe_{1-x}$/Si four-terminal tandem configuration. The surface roughness of the $CdSe_xTe_{1-x}$ layer is measured by atomic force microscopy (AFM) and imported directly into the FDTD simulations. Figure 1(b) compares the experimentally measured and modeled sub-band-gap transmittance through the top cell. The simulation and experiment show reasonable agreement, with the FDTD simulation underestimating the sub-band-gap transmittance. Some

discrepancies are seen in the location of the transmission onset and shape of the transmittance. These are hypothesized to be due to a simplification of the refractive index of the $CdSe_xTe_{1-x}$ in the model, which does not account for the graded CdSe doping at the front interface of the $CdSe_xTe_{1-x}$ absorber layer.

We compare three different roughness cases: one with native texture, a planar surface, and an intermediate case obtained by scaling the surface height of the as deposited texture by 0.5. The transmittance from the simulations without the EVA interlayer is shown in Fig. 2(a). The transmittance spectrum of the planar device supports Fabry-Perot modes that closely match transfer-matrix method predictions. The rough surface has the least transmission, but reducing the roughness of the $CdSe_xTe_{1-x}$ surface results in significant increases to transmittance. However, the proposed four-terminal $CdSe_xTe_{1-x}$/Si tandem cell has an EVA encapsulant interlayer instead of an air gap, so we additionally perform calculations of transmittance into EVA [Fig. 2(b)]. The two rough samples now show significantly greater transmittance, and the differences in transmittance between the samples is less dramatic, indicating that the roughness driven transmission decreases are mitigated via the inclusion of the EVA layer.

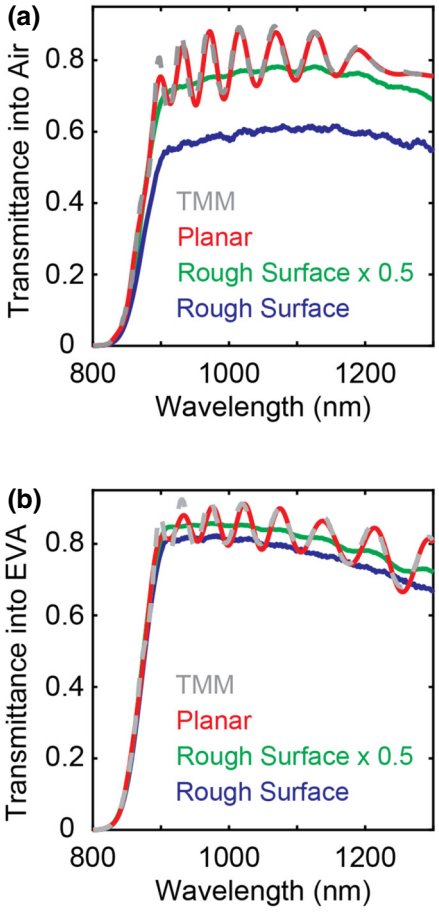

FIG. 2. CdTe solar cell transmittance into (a) air and (b) EVA.

To understand the dominant transparency loss mechanisms, we calculate the wavelength dependent absorption and reflection for the three $CdSe_xTe_{1-x}$ devices with and without the EVA (Fig. 3). The power absorbed is calculated according to Eq. (1), where ε'' is the imaginary part of the complex permittivity, and $|E|^2$ is the intensity of the electric field:

$$P_{\text{abs}} = -0.5\omega|E|^2\varepsilon''. \tag{1}$$

These calculations are performed for the entire three-dimensional (3D) simulation and the power absorbed in each material is isolated, as described in Sec. IV. The front contact of silicon is not included in these simulations, as the focus is on increasing transparency into EVA or air before the light reaches the silicon cell.

At wavelengths longer than the $CdSe_xTe_{1-x}$ band gap, the dominant loss mechanisms are reflection, scattering, and absorption from the front and back TCOs. For all samples, both the reflection and TCO absorption decrease with the inclusion of the EVA interlayer, and the decrease is most significant for the samples with higher roughness. The reduced index contrast between the back TCO and EVA compared to the TCO-air interface reduces both specular reflection and backscattering, and therefore, also front TCO absorption. Planarization of the surface texture decreases both reflection and TCO absorption. Decreasing the $CdSe_xTe_{1-x}$ surface roughness reduces the total reflection because there is less backscattering at the back TCO interface. The increased backscattering from the rough back TCO also leads to increased front TCO absorption, because more light is trapped in the $CdSe_xTe_{1-x}$ cell similar to the roughness induced light trapping utilized in silicon solar cells [35–37].

To understand the roughness induced absorption enhancement in the back TCO, Fig. 4 shows a vertical cross section of the electric field intensity and absorption at a wavelength of 1 μm. As expected, absorption losses are confined to the front and back TCOs. However, the magnitude of the absorption losses varies significantly with surface texture and inclusion of the EVA interlayer. The electric field intensity figures show electric field intensity localization surrounding the peaks of mesoscale (1–3 μm) features on the rough $CdSe_xTe_{1-x}$ surface. These intense electric field concentrations are accompanied by photon jets that extend into the air-EVA interface. Significant interference patterns throughout the cell are due to the superposition of the incoming, reflected, and scattered plane waves.

To visualize the electric field localization and absorption enhancement in the back TCO from a different perspective, we integrate the power absorption over the thickness of the conformal back TCO, average the results from 950

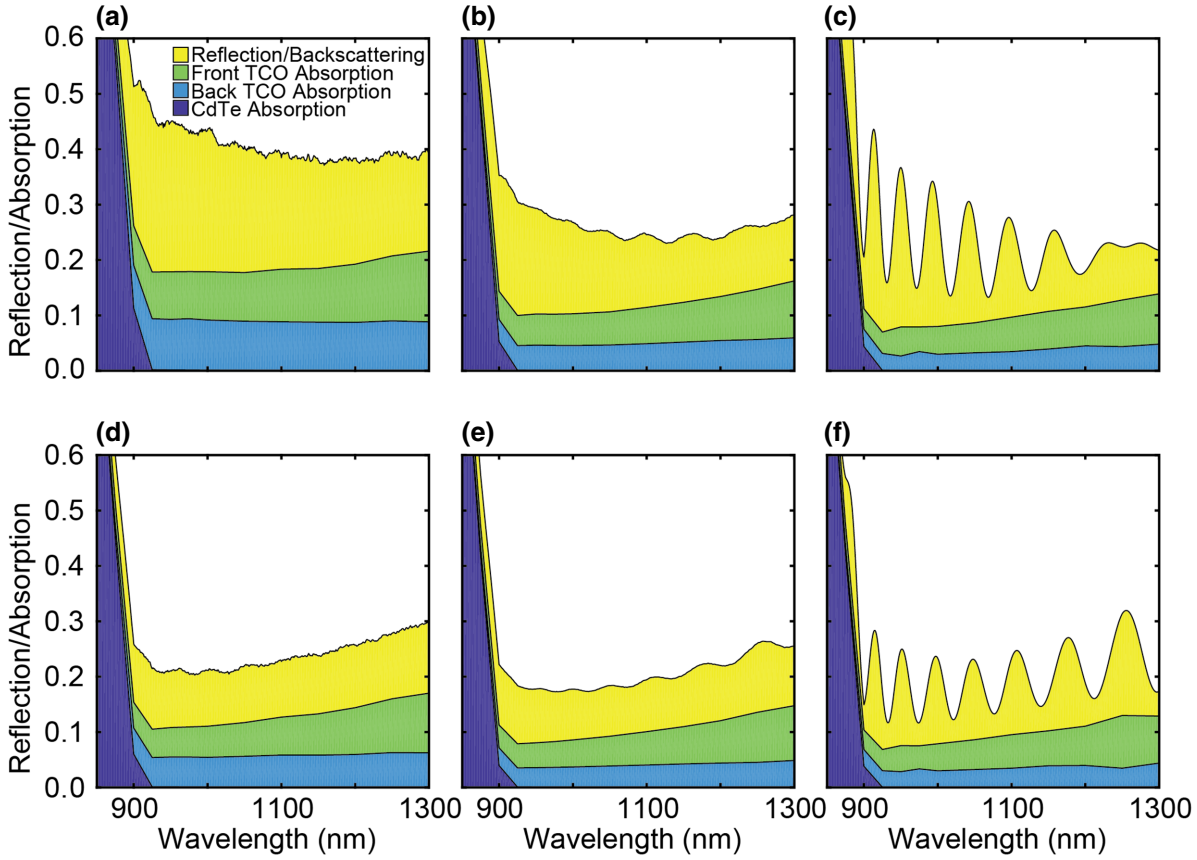

FIG. 3. Dominant optical loss mechanisms preventing sub-band-gap $CdSe_xTe_{1-x}$ cell transmission into (a)–(c) air or (d)–(f) EVA forsamples with (a),(d) a rough surface; (b),(e) a rough surface $\times 0.5$; and (c),(f) a planar surface.

to 1300 nm weighted by the AM1.5 global solar spectrum, and plot the lateral 2D projections in Fig. 5. It is important to recognize that the back TCO thickness remains constant at 150 nm, regardless of surface height. Comparing these calculations to the surface height maps shows that the surface morphology influences the local power absorption in the back TCO: the locations with greatest power absorption are regions of high surface height. This is additionally illustrated in Fig. S2 within the Supplemental Material [34]. At the apex of a mesoscale morphological feature, there is a region of electric field intensity localization and enhanced power absorption. Similar features are seen in the sample with reduced surface roughness, but with decreased magnitude of absorbed power, due to the decreased feature height.

We attribute the electric field intensity localization and absorption enhancement to a focusing effect dominated by the mesoscale features on the $CdSe_xTe_{1-x}$ surface. It is similar to the nonresonant effect seen in previous studies on dielectric particles and gratings, where light is localized near the forward direction surface of the dielectric material [38–46]. The focusing effect is a function of feature size and shape, aspect ratio, index contrast, and wavelength of light. In our case, the average size of the curved surface features is approximately 0.97 μm, which is similar in length to the wavelength range of interest (see Fig. S3 within the Supplemental Material [34]). The reflection and scattering of the injected plane wave off these curved surfaces cause constructive interference that focuses and localizes light around the apex of the surface features. These features are not perfectly optimized to focus the incoming light, but the collective local absorption enhancement leads to a global increase in back TCO absorption by about 141% for the samples that interface with air and about 65% for samples with the EVA interlayer.

The EVA interlayer reduces the magnitude of the back TCO absorption enhancement (and increases transmission) because it reduces the index contrast at the rough surface. Previous studies on dielectric spheres and particles demonstrate that a reduced index contrast shifts the point of focus forward into the lower index medium and creates more forward scattering [39,40,43,44,46]. Similarly, the EVA interlayer enhances forward scattering and decreases lateral scattering, which diminishes the localized absorption enhancement in the back TCO.

This poses the question as to whether further reductions in index contrast could provide even greater enhancement

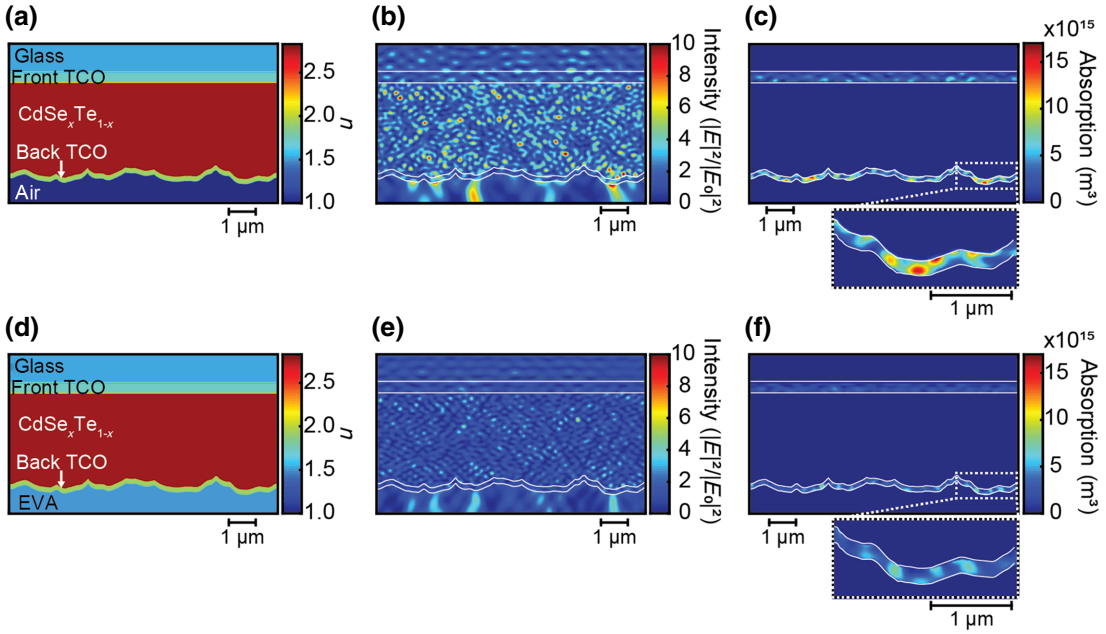

FIG. 4. (a),(d) Cross section of the real component of the refractive index; (b),(e) electric field intensity enhancement; and power absorption in the CdTe solar cell with (a)–(c) air and (d)–(f) EVA. White lines are included in (b),(c),(e),(f) at material interfaces.

to $CdSe_xTe_{1-x}$ cell transmittance. To investigate this, two lossless constant refractive index optical coatings are investigated with slightly different functionalities. First, an $n = 1.7$ optical coating is considered to provide a smaller stepwise transition in refractive index from the back TCO to the EVA interlayer. The second optical coating considered has a larger refractive index of $n = 1.9$, which index matches the back TCO at a wavelength of 1 μm.

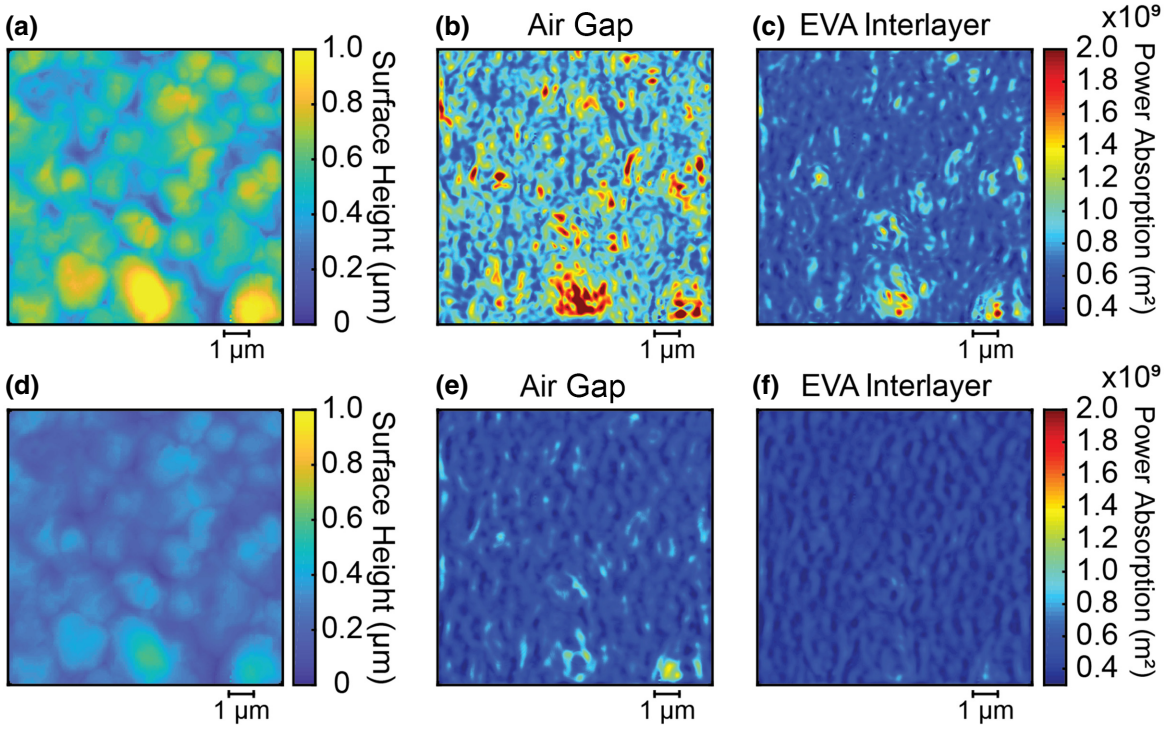

FIG. 5. Surface height profiles and position resolved back TCO power absorption for $CdSe_xTe_{1-x}$ solar cells with (a)–(c) the rough surface (d)–(f) and the rough surface $\times 0.5$. Back TCO power absorption is shown for cells with both (b),(e) air and (c),(f) EVA.

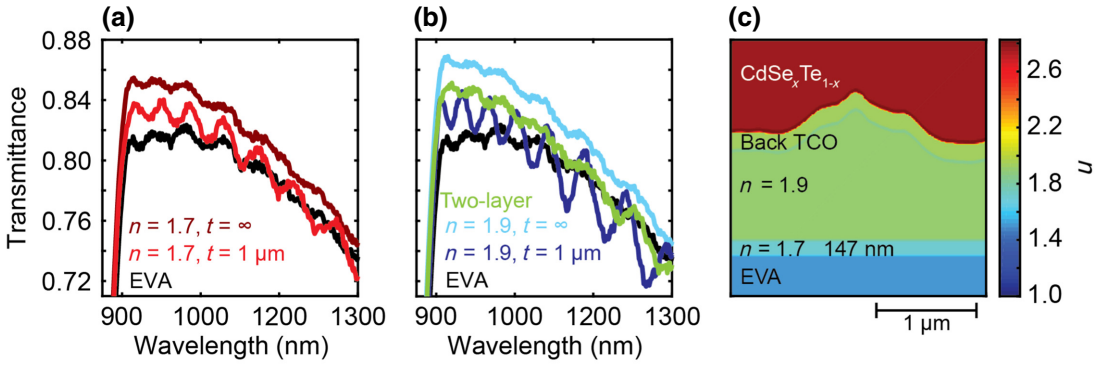

FIG. 6. $CdSe_xTe_{1-x}$ cell transmittance from FDTD simulations for (a) the $n = 1.7$ coatings and (b) the $n = 1.9$ coating and the two-layer coating. (c) Cross section of the refractive index for the two-layer coating.

The effects of including high index optical coatings on the transmittance of a $CdSe_xTe_{1-x}$ cell are summarized in Fig. 6. The transmittance of the solar cell with only EVA is also included as a reference. Semi-infinitely thick optical coatings are first considered to view the effects the coatings have on the unpolished cell's sub-band-gap transmittance without the additional coating-EVA interface. As anticipated, the reduced index contrast results in increases in transmittance beyond devices with the EVA interlayer. The cells with the $n = 1.9$ optical coating have a larger transmittance than those with the $n = 1.7$ coating at shorter wavelengths, but their transmittance is comparable at wavelengths greater than 1050 nm due to dispersion in the refractive index of the back TCO, which disrupts the index matching condition of the $n = 1.9$ coating. These results indicate that substitution of the EVA interlayer with a higher refractive index alternative, such as the high refractive index polymers often used to encapsulate light-emitting diodes [47–50], could be used to further enhance the optical coupling in CdTe/Si four-terminal tandem cells.

The effects of the additional coating-EVA interface are also simulated with 1-μm-thick optical coatings. The coatings are assumed to optically "flatten" the back contact by forming a planar interface with the EVA interlayer. Unfortunately, the transmittance for the devices is reduced due to reflection at the coating-EVA interface. The device with the $n = 1.9$ coating has the largest reduction in transmittance, decreasing below the $CdSe_xTe_{1-x}$ device without an optical coating at longer wavelengths due to its high refractive index contrast with the EVA interlayer. The $CdSe_xTe_{1-x}$ cell with an $n = 1.7$ coating displays a smaller reduction in transmittance and still outperforms the cell without a high index coating at most wavelengths due to its smaller stepwise transitions in refractive index.

The reflection losses at the coating-EVA interface can be significantly reduced by applying an additional coating to serve as an antireflection coating between the two layers. The proposed two-layer optical coating is schematically depicted in Fig. 6(c), consisting of a 1-μm-thick $n = 1.9$ coating to planarize the back contact followed by a $n = 1.7$ coating, the thickness of which, 147 nm, is selected to serve as a quarter-wave layer. The two-layer optical coating outperforms devices with single-layer coatings at short wavelengths. However, dispersion in the back TCO's refractive index causes poor index matching between the $n = 1.9$ optical coating and back TCO at long wavelengths, causing the two-layer coating device's transmittance to fall below the cell with only an EVA interlayer at wavelengths longer than 1100 nm.

After demonstrating improved transmittance through the $CdSe_xTe_{1-x}$ cell, we estimate the performance of the Si cell implemented as the bottom subcell. For this estimate, we assume an industrial p-type mono-PERC silicon cell with an efficiency of 22%. The external quantum efficiency (η_{EQE}) is sourced from the literature [51]. The short circuit current density (J_{SC}) of the Si cell is calculated by

$$J_{SC} = q \int \eta_{EQE}(\lambda) \times T(\lambda) \times \Phi_s(\lambda) d\lambda, \tag{2}$$

where T is the $CdSe_xTe_{1-x}$ solar cell's transmittance, Φ_s is the spectral solar photon flux, and q is the elementary charge. Equation (2) is integrated across the entire AM1.5G solar spectrum, and the results are displayed in Table I.

The J_{SC} for the Si cell under an unfiltered solar spectrum is estimated to be 40.9 mA/cm^2. The open circuit voltage, fill factor, and efficiency of the silicon cell under the $CdSe_xTe_{1-x}$ device can then be calculated according to methods described in the Supplemental Material [34]. The efficiency estimates assume that differences in surface roughness are only influencing the optical properties. Surface texture and other defects like lattice distortions, impurities, and dislocations can impact the material properties, electrical performance, and solar cell efficiency [52–56]. However, isolating the influence of the texture on optics alone allows us to make meaningful performance

TABLE I. Short circuit current density and efficiency of the monosilicon passivated emitter and rear contact (PERC) solar cell (η_{Si}) under different $CdSe_xTe_{1-x}$ solar cell samples and interlayers. The estimated tandem cell efficiency is also included (η_T).

Sample	J_{SC} (mA/cm^2)	η_{Si} (%)	η_T (%)
Rough surface air	5.7	3.0	25.0
Rough surface $\times$0.5 air	7.4	4.0	26.0
Planar air	7.7	4.1	26.1
Rough surface EVA	8.0	4.3	26.3
Rough surface $\times$0.5 EVA	8.4	4.5	26.5
Planar EVA	8.4	4.5	26.5
Two-layer	8.2	4.4	26.4

comparisons between the planarized samples and the high index optical coatings.

Both strategies increase the efficiency of the bottom Si cell. Planarizing the back contact interface results in an increase of 1.1% in silicon cell efficiency with no EVA interlayer, and a 0.2% increase with the interlayer included. Applying the two-layer high index optical coating also results in a slight increase in efficiency for the cell compared to the cell with only EVA. We note that these Si cell efficiencies are similar to those predicted by Tamboli *et al*., and when combined with the CdTe cell efficiency of 22% would exceed a single junction efficiency up to 26.5% [6,57].

III. CONCLUSION

CdTe/Si four-terminal tandem solar cells are promising architectures that take advantage of the two most dominant single junction technologies on the market. This study characterizes the sub-band-gap transparency losses in the $CdSe_xTe_{1-x}$ top cell and investigates two methods to increase top cell transmittance: reducing the roughness and including high index interlayers. The loss in the back TCO is increased by mesoscale features on the $CdSe_xTe_{1-x}$ surface that create a focusing effect and localized absorption enhancement. Since this effect is related to both the height of the surface features and the index contrast, either planarization of the surface texture or the inclusion of higher index optical coatings mitigates the roughness induced optical losses and promote transmittance. A two-layer coating provides a 2%–3% increase in transmittance from 900 to 1000 nm compared to EVA alone.

IV. METHODS

A. Samples

The solar cell samples are provided by First Solar.

B. Surface roughness characterization

Contact mode AFM measurements are performed with a Bruker Dimension ICON atomic force microscope on the back surface of a completed $CdSe_xTe_{1-x}$ solar cell without EVA encapsulation. The total scan area is 15×15 μm^2.

C. UV/vis spectrophotometry

Total transmission measurements are performed using a Cary 7000 UV-vis spectrophotometer with a diffuse reflectance accessory. During the measurement, the $CdSe_xTe_{1-x}$ solar cell is mounted on the integrating sphere transmission port and a polytetrafluoroethylene reflectance standard blocks the back port.

D. FDTD simulations

The simulated $CdSe_xTe_{1-x}$ solar cell consists of a 330-nm-thick front TCO on a glass substrate, a 3.3-μm-thick $CdSe_xTe_{1-x}$ layer, and a 150-nm-thick back TCO. The front and back transparent TCO contacts are multilayer stacks with additional layer thicknesses between 10 and 40 nm thick. A 35-nm-thick ZnTe layer serves as a p contact on top of the graded $CdSe_xTe_{1-x}$ absorber. Surface roughness data from the AFM measurements are applied to the $CdSe_xTe_{1-x}$ layer and all layers in the transparent back contact. A simulation area of 10×10 μm^2 with periodic boundary conditions is found to be sufficiently large to capture the surface roughness.

The optical simulations are conducted by injecting a plane wave into the $CdSe_xTe_{1-x}$ solar cell, starting with the glass layer. A monitor in the air gap or EVA interlayer is used to collect the transmittance through the device stack, and 3D electric field monitors placed around the entire device are used to calculate absorption. When comparing the simulated transmission to experimental measurements, reflection loss off the air-glass interface and absorption loss through the 2.65-mm-thick glass substrate is added to the simulation results in postprocessing. The reflection at normal incidence is estimated with Fresnel equations and is about 4%, and the glass absorption estimated with Beer's law is about 2%.

ACKNOWLEDGMENTS

This work was supported by First Solar Inc. Part of this work was performed in the College of Science and Engineering Characterization Facility, University of Minnesota, which received capital funding from the NSF through the MRSEC (Grant No. DMR-2011401) and the NNCI (Grant No. ECCS-2025124) programs. Part of this work was carried out with equipment supported by funding from the National Science Foundation through the UMN MRSEC under Grant No. DMR-2011401. The authors acknowledge the Minnesota Supercomputing Institute (MSI) at the University of Minnesota for providing resources that contributed to the research results reported within this manuscript.

All authors contributed to the concept and design of experiments and simulations. J.K. and B.M.C. conducted UV/vis spectrophotometry measurements, AFM measurements, and FDTD simulations and data processing under the guidance of V.E.F. V.C. and A.L. provided the $CdSe_xTe_{1-x}$ solar cell samples and expertise on photovoltaic device fabrication and characterization. J.K. and V.E.F. drafted the manuscript, with input from all authors.

[1] G. M. Wilson, *et al.*, The 2020 photovoltaic technologies roadmap, J. Phys. Appl. Phys. **53**, 493001 (2020).

[2] F. Martinho, Challenges for the future of tandem photovoltaics on the path to terawatt levels: A technology review, Energy Environ. Sci. **14**, 3840 (2021).

[3] P. J. Verlinden, Future challenges for photovoltaic manufacturing at the terawatt level, J. Renewable Sustainable Energy **12**, 053505 (2020).

[4] M. Yamaguchi, K.-H. Lee, K. Araki, and N. Kojima, A review of recent progress in heterogeneous silicon tandem solar cells, J. Phys. Appl. Phys. **51**, 133002 (2018).

[5] C. Ballif, F.-J. Haug, M. Boccard, P. J. Verlinden, and G. Hahn, Status and perspectives of crystalline silicon photovoltaics in research and industry, Nat. Rev. Mater. **7**, 8 (2022).

[6] A. C. Tamboli, D. C. Bobela, A. Kanevce, T. Remo, K. Alberi, and M. Woodhouse, Low-cost CdTe/silicon tandem solar cells, IEEE J. Photovoltaics **7**, 1767 (2017).

[7] J. Werner, B. Niesen, and C. Ballif, Perovskite/silicon tandem solar cells: Marriage of convenience or true love story? – An overview, Adv. Mater. Interfaces **5**, 1700731 (2018).

[8] M. Carmody, S. Mallick, J. Margetis, R. Kodama, T. Biegala, D. Xu, P. Bechmann, J. W. Garland, and S. Sivananthan, Single-crystal II-VI on Si single-junction and tandem solar cells, Appl. Phys. Lett. **96**, 153502 (2010).

[9] G. M. Hanket, B. E. McCandless, W. A. Buchanan, S. Fields, and R. W. Birkmire, Design of a vapor transport deposition process for thin film materials, J. Vac. Sci. Technol., A **24**, 1695 (2006).

[10] T. Ablekim, Joel N. Duenow, Xin Zheng, Helio Moutinho, John Moseley, Craig L. Perkins, Steven W. Johnston, Patrick O'Keefe, Eric Colegrove, David S. Albin, Matthew O. Reese, and Wyatt K. Metzger, Thin-film solar cells with 19% efficiency by thermal evaporation of CdSe and CdTe, ACS Energy Lett. **5**, 892 (2020).

[11] A. Romeo, E. Artegiani, and D. Menossi, Low substrate temperature CdTe solar cells: A review, Sol. Energy **175**, 9 (2018).

[12] F. He, J. Li, S. Lin, W. Long, L. Wu, X. Hao, J. Zhang, and L. Feng, Semitransparent CdTe solar cells with $CdCl_2$ treated absorber towards the enhanced photovoltaic conversion efficiency, Sol. Energy **214**, 196 (2021).

[13] S. Chander and M. S. Dhaka, Optimization of physical properties of vacuum evaporated CdTe thin films with the application of thermal treatment for solar cells, Mater. Sci. Semicond. Process. **40**, 708 (2015).

[14] S. Chander and M. S. Dhaka, Physical properties of vacuum evaporated CdTe thin films with post-deposition thermal annealing, Phys. E (Amsterdam, Neth.) **73**, 35 (2015).

[15] M. Isah, K. S. Rahman, C. Doroody, M. N. Harif, H. N. Rosly, K. Sopian, S. K. Tiong, and N. Amin, Design optimization of CdTe/Si tandem solar cell using different transparent conducting oxides as interconnecting layers, J. Alloys Compd. **870**, 159351 (2021).

[16] A. Rouhbakhshmeghrazi and M. Madadi, Novel design of polycrystalline CdTe/Si tandem solar cells using SiO_2/TiO_2 distributed Bragg reflector, Tecciencia **15**, 67 (2020).

[17] M. Jošt, L. Kegelmann, L. Korte, and S. Albrecht, Monolithic perovskite tandem solar cells: A review of the present status and advanced characterization methods toward 30% efficiency, Adv. Energy Mater. **10**, 1904102 (2020).

[18] J. P. Mailoa, M. Lee, I. M. Peters, T. Buonassisi, A. Panchula, and D. N. Weiss, Energy-yield prediction for II–VI-based thin-film tandem solar cells, Energy Environ. Sci. **9**, 2644 (2016).

[19] W. Qarony, M. I. Hossain, V. Jovanov, A. Salleo, D. Knipp, and Y. H. Tsang, Influence of perovskite interface morphology on the photon management in perovskite/silicon tandem solar cells, ACS Appl. Mater. Interfaces **12**, 15080 (2020).

[20] F. M. T. Enam, K. S. Rahman, M. I. Kamaruzzaman, K. Sobayel, P. Chelvanathan, B. Bais, M. Akhtaruzzaman, A. R. M. Alamoud, and N. Amin, Design prospects of cadmium telluride/silicon (CdTe/Si) tandem solar cells from numerical simulation, Optik **139**, 397 (2017).

[21] X. Wu, J. Zhou, A. Duda, J. C. Keane, T. a Gessert, Y. Yan, and R. Noufi, 13·9%-efficient CdTe polycrystalline thin-film solar cells with an infrared transmission of ∼50%, Prog. Photovoltaics Res. Appl. **14**, 471 (2006).

[22] J. Li, F. He, X. Hao, S. Lin, W. Long, T. Gan, L. Wu, J. Zhang, and L. Feng, Semitransparent CdTe solar cell with over 70% near-infrared transmittance, J. Mater. Sci. Mater. Electron. **31**, 18198 (2020).

[23] X. Wen, Z. Lu, X. Sun, Y. Xiang, Z. Chen, J. Shi, I. Bhat, G.-C. Wang, M. Washington, and T.-M. Lu, Epitaxial CdTe thin films on mica by vapor transport deposition for flexible solar cells, ACS Appl. Energy Mater. **3**, 4589 (2020).

[24] O. Toma, L. Ion, M. Girtan, and S. Antohe, Optical, morphological and electrical studies of thermally vacuum evaporated CdTe thin films for photovoltaic applications, Sol. Energy **108**, 51 (2014).

[25] J. M. Kestner, S. McElvain, S. Kelly, T. R. Ohno, L. M. Woods, and C. A. Wolden, An experimental and modeling analysis of vapor transport deposition of cadmium telluride, Sol. Energy Mater. Sol. Cells **83**, 55 (2004).

[26] B. McCandless, W. Buchanan, G. Sriramagiri, C. Thompson, J. Duenow, D. Albin, S. A. Jensen, J. Moseley, M. Al-Jassim, and W. K. Metzger, Enhanced p-type doping in polycrystalline CdTe films: Deposition and activation, IEEE J. Photovoltaics **9**, 912 (2019).

[27] X. Wu, High-efficiency polycrystalline CdTe thin-film solar cells, Sol. Energy **77**, 803 (2004).

[28] B. E. McCandless, R. W. Birkmire, and W. A. Buchanan, in *Conference Record of the Twenty-Ninth IEEE Photovoltaic Specialists Conference, 2002* (2002), pp. 547–550.

[29] R. S. Yavorskyi, Features of optical properties of high stable CdTe photovoltaic absorber layer, Phys. Chem. Solid State **21**, 2 (2020).

[30] M. A. Islam, Q. Huda, M. S. Hossain, M. M. Aliyu, M. R. Karim, K. Sopian, and N. Amin, High quality 1 μm thick CdTe absorber layers grown by magnetron sputtering for solar cell application, Curr. Appl. Phys. **13**, S115 (2013).

[31] R. Yavorskyi, L. Nykyruy, G. Wisz, P. Potera, S. Adamiak, and Sz. Górny, Structural and optical properties of cadmium telluride obtained by physical vapor deposition technique, Appl. Nanosci. **9**, 715 (2019).

[32] S. K. Pandey, U. Tiwari, R. Raman, C. Prakash, V. Krishna, V. Dutta, and K. Zimik, Growth of cubic and hexagonal CdTe thin films by pulsed laser deposition, Thin Solid Films **473**, 54 (2005).

[33] H. M. Al-Allak, A. W. Brinkman, H. Richter, and D. Bonnet, Dependence of {CdS}/{CdTe} thin film solar cell characteristics on the processing conditions, J. Cryst. Growth **159**, 910 (1996).

[34] See the Supplemental Material at http://link.aps.org/supplemental/10.1103/PRXEnergy.2.023004 for optical constants of materials in the $CdSe_xTe_{1-x}$ solar cell, the relationship between power absorption and surface height, Si efficiency estimation methods, and surface feature size analysis.

[35] J. Müller, B. Rech, J. Springer, and M. Vanecek, TCO and light trapping in silicon thin film solar cells, Sol. Energy **77**, 917 (2004).

[36] M. A. Green, Lambertian light trapping in textured solar cells and light-emitting diodes: Analytical solutions, Prog. Photovoltaics Res. Appl. **10**, 235 (2002).

[37] H. Sai, Y. Kanamori, K. Arafune, Y. Ohshita, and M. Yamaguchi, Light trapping effect of submicron surface textures in crystalline Si solar cells, Prog. Photovoltaics Res. Appl. **15**, 415 (2007).

[38] J. F. Owen, R. K. Chang, and P. W. Barber, Internal electric field distributions of a dielectric cylinder at resonance wavelengths, Opt. Lett. **6**, 540 (1981).

[39] D. S. Benincasa, P. W. Barber, J.-Z. Zhang, W.-F. Hsieh, and R. K. Chang, Spatial distribution of the internal and near-field intensities of large cylindrical and spherical scatterers, Appl. Opt. **26**, 1348 (1987).

[40] O. V. Minin and I. V. Minin, Optical phenomena in mesoscale dielectric particles, Photonics **8**, 12 (2021).

[41] P. Chýlek, J. D. Pendleton, and R. G. Pinnick, Internal and near-surface scattered field of a spherical particle at resonant conditions, Appl. Opt. **24**, 3940 (1985).

[42] C. Rockstuhl, F. Lederer, K. Bittkau, and R. Carius, Light localization at randomly textured surfaces for solar-cell applications, Appl. Phys. Lett. **91**, 171104 (2007).

[43] A. Heifetz, S.-C. Kong, A. V. Sahakian, A. Taflove, and V. Backman, Photonic nanojets, J. Comput. Theor. Nanosci. **6**, 1979 (2009).

[44] A. Darafsheh, Photonic nanojets and their applications, J. Phys. Photonics **3**, 022001 (2021).

[45] C.-Y. Liu, O. V. Minin, and I. V. Minin, First experimental observation of array of photonic jets from saw-tooth phase diffraction grating, EPL Europhys. Lett. **123**, 54003 (2018).

[46] S. Lecler, Y. Takakura, and P. Meyrueis, Properties of a three-dimensional photonic jet, Opt. Lett. **30**, 2641 (2005).

[47] E. K. Macdonald and M. P. Shaver, Intrinsic high refractive index polymers, Polym. Int. **64**, 6 (2015).

[48] J. Liu and M. Ueda, High refractive index polymers: Fundamental research and practical applications, J. Mater. Chem. **19**, 8907 (2009).

[49] H.-J. Yen and G.-S. Liou, A facile approach towards optically isotropic, colorless, and thermoplastic polyimidothioethers with high refractive index, J. Mater. Chem. **20**, 4080 (2010).

[50] F. W. Mont, J. K. Kim, M. F. Schubert, E. F. Schubert, and R. W. Siegel, High-refractive-index TiO_2-nanoparticle-loaded encapsulants for light-emitting diodes, J. Appl. Phys. **103**, 083120 (2008).

[51] F. Ye, W. Deng, W. Guo, R. Liu, D. Chen, Y. Chen, Y. Yang, N. Yuan, J. Ding, Z. Feng *et al.*, in *2016 IEEE 43rd Photovoltaic Specialists Conference (PVSC)* (2016), pp. 3360–3365.

[52] A. Goktas, E. Aslan, F. Arslan, and A. Kilic, Characterization of multifunctional solution-processed $Sn_{1-x}Zn_xS$ nanostructured thin films for photosensitivity and photocatalytic applications, Opt. Mater. **133**, 112984 (2022).

[53] A. Tumbul, A. Göktaş, M. Z. Zarbali, and F. Aslan, Structural, morphological and optical properties of the vacuum-free processed CZTS thin film absorbers, Mater. Res. Express **5**, 066408 (2018).

[54] B. Zhou, X. Yin, J. Zhang, G. Zeng, B. Li, J. Zhang, and L. Feng, Numerical simulation of an innovative high efficiency solar cell with CdTe/Si composite absorption layer, Opt. Mater. **110**, 110505 (2020).

[55] H. Gencer, A. Goktas, M. Gunes, H. I. Mutlu, and S. Atalay, Electrical transport and magnetoresistance properties of $La_{0.67}Ca_{0.33}MnO_3$ film coated on Pyrex glass substrate, Int. J. Mod. Phys. B **22**, 497 (2008).

[56] F. Mikailzade, H. Türkan, F. Önal, M. Zarbali, A. Göktaş, and A. Tumbul, Structural and magnetic properties of polycrystalline $Zn_{1-x}Mn_xO$ films synthesized on glass and p-type Si substrates using sol–gel technique, Appl. Phys. A **127**, 408 (2021).

[57] M. A. Green, E. D. Dunlop, J. Hohl-Ebinger, M. Yoshita, N. Kopidakis, and X. Hao, Solar cell efficiency tables (version 56), Prog. Photovoltaics Res. Appl. **28**, 629 (2020).